https://doi.org/10.1016/j.engstruct.2022.115392

Machine learning (ML) based models for predicting the ultimate strength of rectangular concrete-filled steel tube (CFST) columns under eccentric loading

Chen Wang[1], Tak-Ming Chan[1, *]

[1]Dept. of Civil and Environmental Engineering, The Hong Kong Polytechnic Univ., Hung Hom, Hong Kong.
[*] Email: tak-ming.chan@polyu.edu.hk

Abstract

Concrete-filled steel tubes (CFSTs) are popularly used in structural applications. The accurate prediction of their ultimate strength is a key for the safety of the structure. Extensive studies have been conducted on the strength prediction of CFSTs under concentric loading. However, in real situation CFSTs are usually subjected to eccentric loading. The combined compression and bending will result in more complex failure mechanisms at the ultimate strength. The accuracy of methods in design codes is usually limited due to their simplicity. In this study, three machine learning (ML) methods, namely, Support Vector Regression (SVR), Random Forest Regression (RFR), and Neural Networks (NN), are adopted to develop models to predict the ultimate strength of CFSTs under eccentric loading. A database consisting of information of 403 experimental tests from literature is created and statistically analyzed. The database was then split to a training set which was used to optimize and train the ML models, and a test set which was used to evaluate performance of trained ML models. Compared with the methods in two typical design codes, the ML models achieved notable improvement in prediction accuracy. The parametric study revealed that the trained ML models could generally capture the effect of each primary input feature, which was verified by the relevant experimental test results.

Keywords: machine learning, concrete-filled steel tube (CFST), eccentric loading, support vector machine, random forest, neural network

1 Introduction

Concrete-filled steel tube (CFST) columns have been popularly used in high-rise buildings, bridges and many other structural applications as they offer a combination of the advantages of steel and concrete (Zhu & Chan, 2018; Chen et al., 2021). This is mainly attributed to the enhanced performance that is resulted from the interaction between the steel and concrete. Specifically, due to the difference in the Poisson's ratio between steel and concrete, the volume increase of the concrete core is constrained by the exterior steel tube. As a result, both the strength and ductility of the concrete are enhanced. On the other hand, the inward buckling of the steel tube is restrained by the in-filled concrete core.

For the ultimate strength of CFST columns under concentric compressive loading, a large number of experimental tests have been conducted by other researchers. A database of 880 experimental specimens was

compiled in Le et al. (2021) for rectangular CFSTs under concentric compressive loading. Through the extensive studies over the past years, key factors of rectangular CFST columns that affect the ultimate strength under concentric loading have been studied thoroughly. Among them are the slenderness of the steel section, the length of the column, the aspect ratio of the cross section, the volumetric steel-to-concrete ratio, etc., in addition to the material strengths. For instance, the slenderness affects the local stability of the steel tube. The aspect ratio of the cross section and the volumetric steel-concrete ratio are found to affect the confinement condition in the concrete core, and therefore, have an impact on the ultimate strength.

However, in actual condition, CFST columns are expected to carry not only axial loads but also bending moments. With the interaction between compression and bending, the behavior of the composite section will become more complex and various more mechanisms may affect the ultimate strength. Compared with studies on concentric loading, less research has been conducted for the eccentric loading cases or the combined compression and bending in general. A thorough understanding regarding the effect of loading eccentricity on the failure mechanisms requires additional research. Currently, the available design methodologies usually limit their field of application, in regard to material strengths and cross section slenderness, as will be elaborated in Section 4. Moreover, the available methods typically take a relatively simple mathematical formula for convenience of design and considers only a few design parameters, which may not be able to account for all the influential factors.

Machine learning (ML), as a method to realize artificial intelligence, is to explore hidden laws from existing data for prediction or classification. They are good at comprehending complex relationships between influencing geometric and material properties. They have been increasingly applied to solve complex issues in the field of CFSTs. Du et al. (2017) and Tran et al. (2019) adopted an artificial neural network (ANN) to

predict the axial capacity of rectangular CFST under concentric loading. Jayalekshmi et al. (2018) validated an empirical formula for the estimation of the axial strength of circular CFSTs using an ANN. Ren et al. (2019) developed a model to predict the ultimate strength of square CFST using the support vector machine (SVM). It is noted that most ML-based study on CFSTs were focused on the concentric loading condition, as data are the most in this case. The ML-based study on CFSTs subjected to eccentric loading or combined compression and bending in general is limited. Naser et al. (2021) implemented naturally inspired ML algorithms, genetic programming and gene expression programming, to predict the ultimate load of CFSTs under eccentric loading. The potential of various other ML methods has not been fully explored to comprehend the complex behavior of CFSTs under interaction of compression and bending.

This study aims to develop models that can predict the ultimate strength of rectangular CFSTs under eccentric loading accurately and reliably using ML methods. Three ML methods, namely, Support Vector Regression (SVR), Random Forest Regression (RFR), and Neural Network (NN), are implemented in this study. Firstly, a database consisting of information of 403 experimental tests is created and its statistical characteristics are analyzed. Secondly, fundamentals of the three adopted ML methods are briefly presented to illustrate how they solve complex regression problems. Thirdly, a model training procedure that includes train-test data split, feature scaling, hyperparameter optimization, is implemented to obtain the optimized and trained models. Fourthly, the performance of the trained ML models is evaluated and compared with the methods in typical design codes. Finally, parametric analyses are conducted to study the effect of each primary input feature using the ML models and code methods.

2 Description of database

A database of 403 experimental tests on rectangular CFST columns under eccentric loading was compiled from the literature, and is described in this section. Table 1 lists the sources from which the experimental data

were collected along with the range of each feature. Figure 1 shows the general test setup and the definitions of the geometric features. To make the features have consistent meaning, the dimensions B and H are defined with regards to the bending axis, with B the outside dimension in parallel with the bending axis and H the outside dimension perpendicular to the bending axis.

Regarding the material properties, two features are collected: yield strength of steel, F_y, and compressive strength of concrete, f_c. The reported compressive strengths of concrete were based on four types of concrete specimens: 100 mm cube ($f_{cu,100}$), 150 mm cube ($f_{cu,150}$), cylinder with 100 mm diameter and 200 mm height ($f_{cy,100}$), and cylinder with 150 mm diameter and 300 mm height ($f_{cy,150}$). In this study, the strength based on cylinder with 150 mm diameter and 300 mm height was adopted as the characteristic compressive strength of concrete, i.e., $f_c = f_{cy,150}$. Conversion of concrete compressive strengths obtained through other specimen types followed the formulas listed in Table 2.

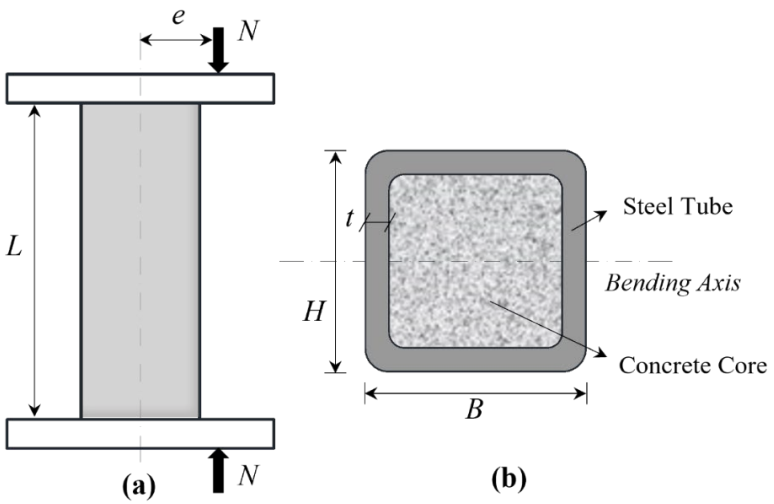

Figure 1 Error! No sequence specified.General test setup and definition of geometric parameters

Table 1 Source and summary of the database

Reference	Year	No. of tests	L (mm)	e (mm)	H (mm)	B (mm)	t (mm)	F_y (MPa)	f_c (MPa)
Li et al.	2021	24	1000-2000	20-65	150	150	4.0	435	101
Zhong et al.	2021	12	386-445	30-70	120-140	120-140	4.9-5.9	718-762	40-113
Huang et al.	2020	6	500	25-75	130	130	5.0	1031	76-125
Li et al.	2018	12	450	20-65	150	150	4.0-6.0	433-437	101

Xiong et al.	2017	3	3640	20-50	200	200	12.0-12.5	465-756	168-174
Du et al.	2017	12	1180	13-41.5	150-200	100-150	8.3	488	36-47
Lee et al.	2017	3	1720	20-40	150-300	300	5.0	301-746	71-84
Liew et al.	2016	3	3640	20-50	200	200	12.0-12.5	465-756	168-174
Qu et al.	2013	9	700-1000	10-70	150-300	100-200	4.0-5.7	242-336	32-57
Hernandez-Figueirido et al.	2012b	12	2135	20-50	100	100-150	4.0-5.0	293-460	26-93
Hernandez-Figueirido et al.	2012a	15	2135-4135	20-50	100-150	100	4.0-5.0	280-460	74-95
Huang et al.	2011	4	950-1850	25-50	160	160	2.5	230	40-42
Long et al.	2008	2	1200	40-70	300	150	6.0	465	46
Yu et al.	2008	4	1500	15-30	100	100	1.9	404	112
Cai et al.	2007	3	1500	40-100	300	300	6.0	382	51
Tao et al.	2007	4	1190-2340	30-60	200	200	2.5	270	50
Zhang & Guo	2007	26	919-3101	0.9-72	125-201	125-200	2.9-4.9	317-319	75
Guo	2006	7	450-1800	20-40	99-201	99-201	3.6	284	42
Liu	2006	20	360-2600	15-60	120-180	90-130	4.0	495	60
Guo et al.	2005	10	921-3101	0.9-3.5	125-150	150-200	2.9-4.9	317-319	75
Chen et al.	2005	2	1958	40-70	200	200	1.25	373	45
Zhang et al.	2004	8	1090-3101	21-43	150	150	2.9-4.9	317-319	75
Fujimoto et al.	2004	21	648	45-300	149-319	149-319	4.4-6.4	262-618	25-77
Guo et al.	2004	8	919-1982	20-72	125-137	174-201	2.9-4.8	316-319	75
Han & Yao	2004	5	2310	30	200	200	3.0	304	50
Liu	2004	12	870-2310	20-70	150-200	80-150	4.2	550	61-72
Han & Yao	2003	12	780-2340	14-31	130	195	2.7	340	17
Mursi & Uy	2004	3	2800	10-20	104-164	104-164	3.0	269	65
Han et al.	2001	21	2183-2223	15-80	120-200	120-200	3.8-5.9	321-330	22-46
Uy	2001	7	330-630	15-50	110-210	110-210	5	784	30-32
Uy	2000	12	360-720	20-100	126-246	126-246	3.0	300	32-50
Wei & Han	2000	21	2600	15-80	120-200	120-200	3.8-5.9	321-330	19-37
Wang & Moore	1997	4	4000	55	80-120	80-120	6.3	370	38
Matsui & Tsuda	1996	18	600-4500	25-125	150	150	4.5	438	32
Grauers	1993	16	1696-3196	10-20	120-250	120-250	5-8	300-439	31-103
Shakir-Khalil & Mouli	1990	1	2940	8	80	120	5.0	358	36
Cederwall et al.	1991	12	3000	10-20	120	120	5.0-8.0	300-439	39-103
Shakir-Khalil & Zeghiche	1989	4	2940-3210	16-60	80-120	80-120	4.5	343-386	33-37
Zhang	1989	18	596-804	30-120	149-201	149-201	3.9-7.8	205-300	43
Bridge	1976	3	2130-3050	38-64	153-204	152-204	6.5-10.0	254-291	30-31
Knowles & Park	1969	4	812-1422	7.6-25.4	76.2	76.2	3.4	324	41
	Total	**403**							

Table 2 Formulas for conversion of concrete strengths

Strength	Conversion formula
$f_{cy,100}$	$f_{cy,150} = 1.67 \times 150^{-0.112} f_{cy,100}$ (Sakino et al., 2004)
$f_{cu,150}$	$f_{cy,150} = \left[0.76 + 0.2 \log_{10}\left(\frac{f_{cu,150}}{19.6}\right)\right] f_{cu,150}$ (Mirza & Lacroix, 2004)
$f_{cu,100}$	$f_{cu,150} = 0.9 \times f_{cu,100}$ (Reineck et al., 2003)

2.1 Statistical properties of the database

Figure 2 shows the scatter plots between each primary input feature and the ultimate strength. In terms of section sizes, most specimens are small to moderate sized mainly due to the limit on the loading capacity. The outside dimensions are generally below 250 mm and thickness of most steel tubes are within the range of 2-8 mm.

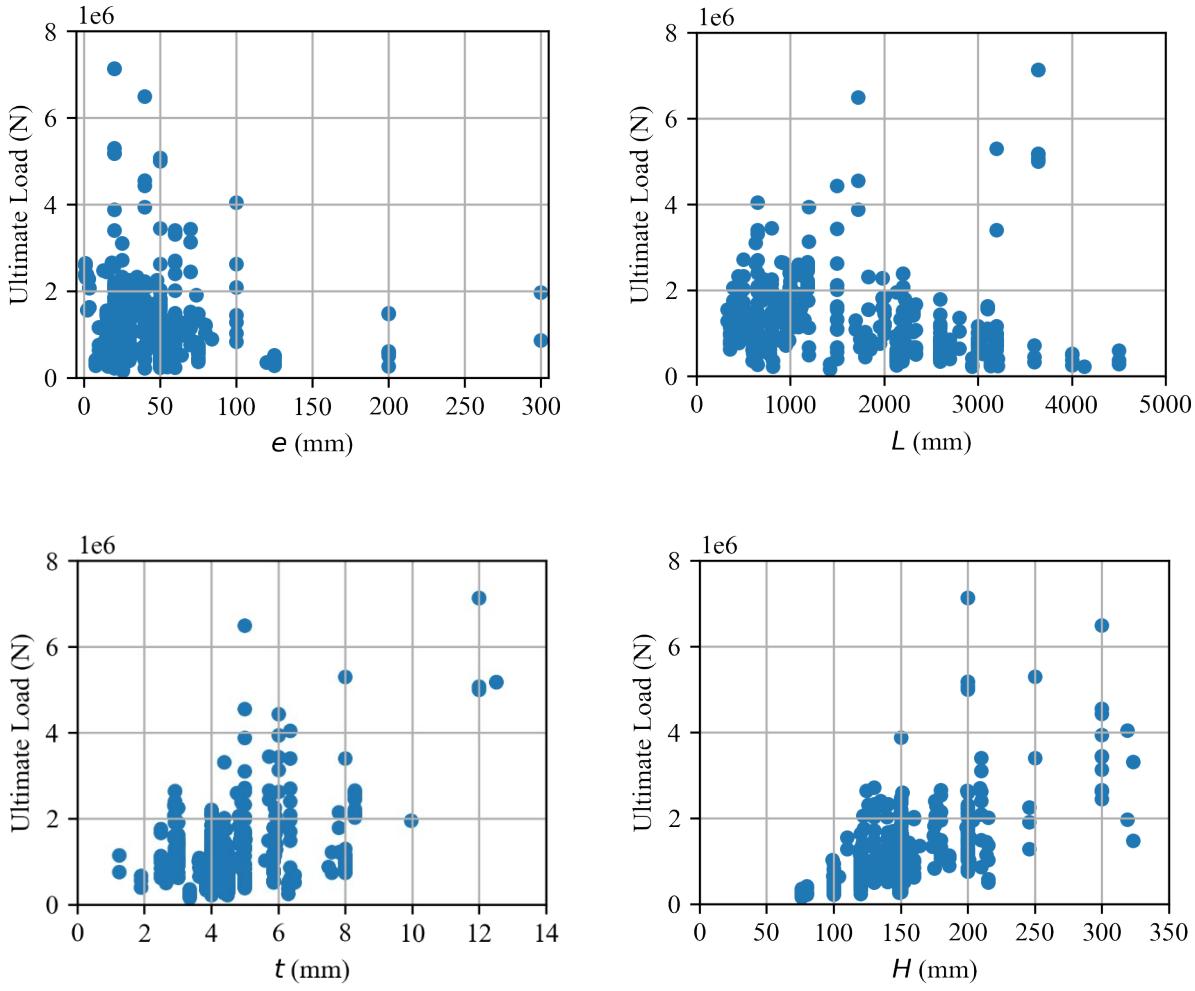

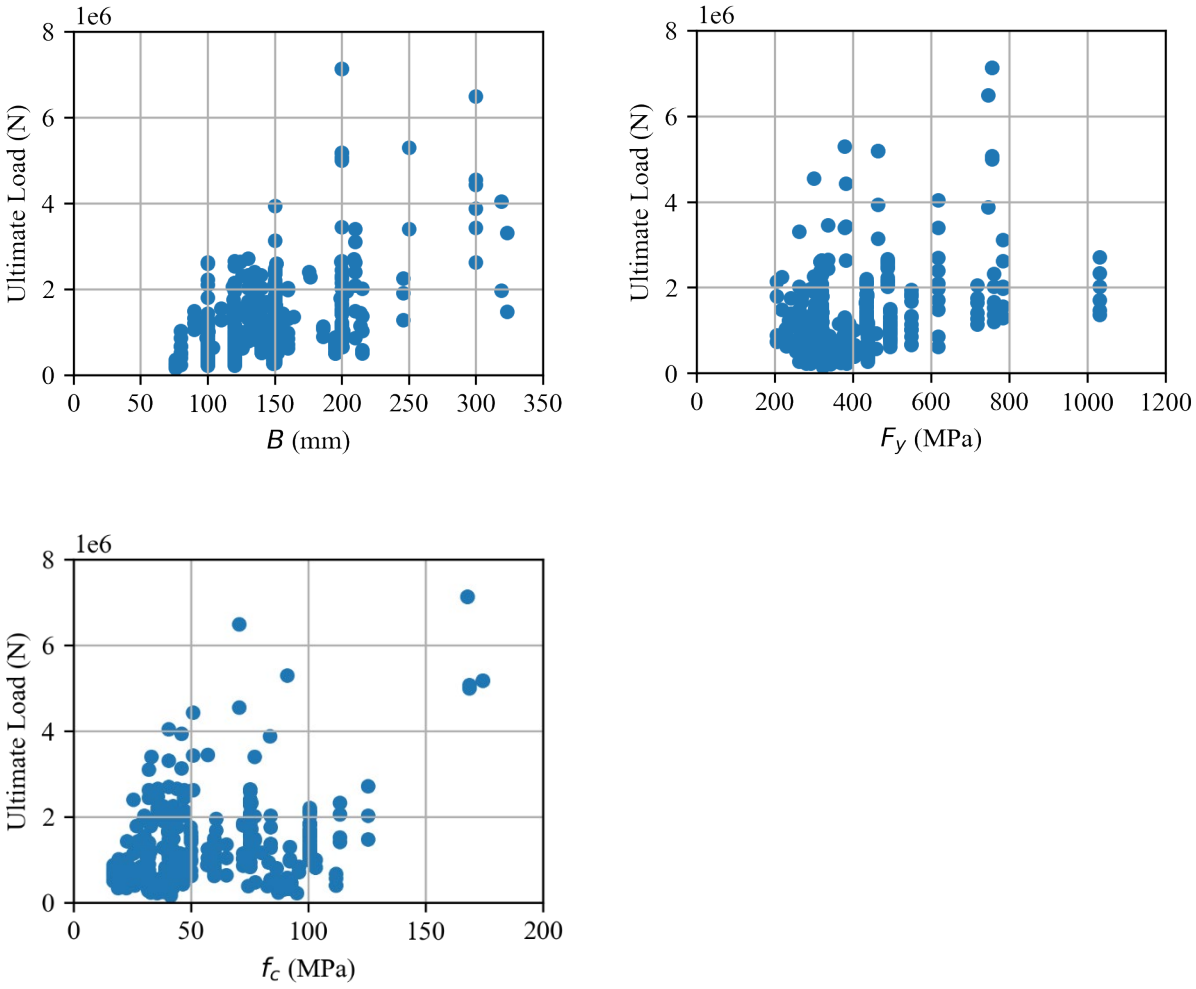

Figure 2 Scatter plots of primary input features against the ultimate strength

Regarding the material strengths, the database covers a wide range for both steel and concrete, with F_y ranging from 200 MPa (mild steel) to 1030 MPa (high-strength steel), f_c ranging from 17 MPa (normal strength concrete) to 174 MPa (high or ultra-high strength concrete). Although wide ranges are covered for material strengths, the data distribution is not even. The steel strength concentrated in the range of 200-800 MPa, with only a few samples above 800 MPa. For concrete strength, most data fall in the range of 20-100 MPa, with a few above 100 MPa.

To further assess the database and provide more information that may be helpful for the training of ML models, 11 secondary features that may be relevant to the ultimate strength are preliminarily considered. The 11 secondary features and their physical implication are listed in Table 3. The statistical distribution of the 11 secondary features is presented in Figure 3. As shown, most specimens experienced low to moderate loading

eccentricity with *e/H* concentrated between 0 and 0.5. Only a small fraction of the specimens experienced large loading eccentricity. The length of the tested specimens ranges from 200 to 4500 mm, but most specimens are short columns with $\bar{\lambda}$ less than 1.0 and only a small number of tested specimens are long columns that failed in the form of global buckling. The parameter of δ is generally used to evaluate the extent of confinement provided by the steel tube to the concrete core. With the values of δ almost evenly distributed over the range of 0.2-0.8, the database is deemed suitable to represent a wide range of confinement of the concrete core.

Table 3 Secondary features preliminarily considered

Secondary feature	Formula and physical implication
A_sF_y	Yield resistance of the steel tube
A_cf_c	Compressive resistance of the concrete core
N_{cr}	Elastic buckling resistance of the composite column based on the effective flexural stiffness of the section
N_{pl}	$A_sF_y + A_cf_c$, plastic resistance of the composite section
$\bar{\lambda}$	$\sqrt{N_{pl}/N_{cr}}$, a measure of slenderness of the composite column
δ	A_sF_y/N_{pl}, a measure of the confinement on the concrete core provided by the steel tube
$EI_{eff,s}$	Effective flexural stiffness of the steel tube section (CEN, 2005)
$EI_{eff,c}$	Effective flexural stiffness of the concrete core section (CEN, 2005)
e/H	A measure of the extent of loading eccentricity
H/B	Aspect ratio of the cross section of the steel tube
H/t	A measure of the cross-section slenderness of the steel tube

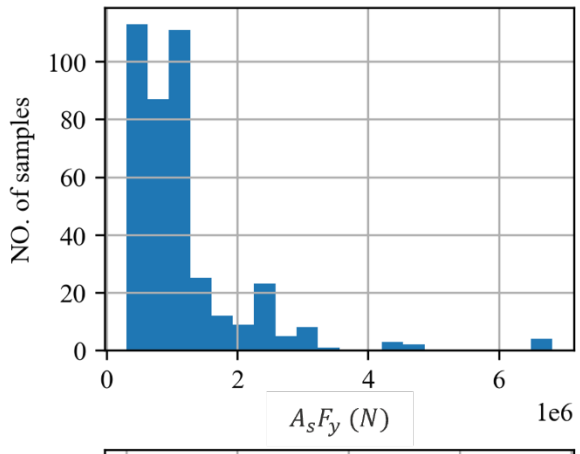
NO. of samples
A_sF_y (N)
1e6

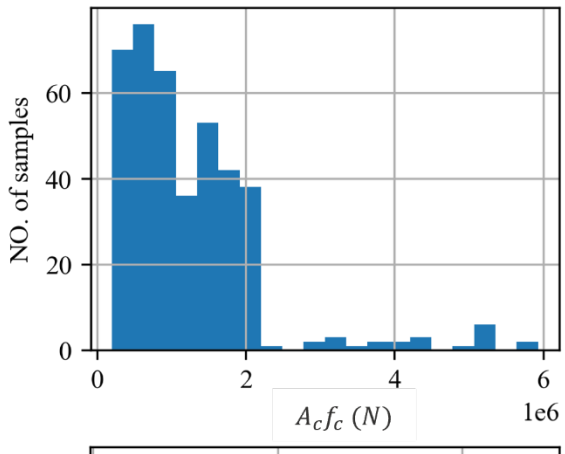
NO. of samples
A_cf_c (N)
1e6

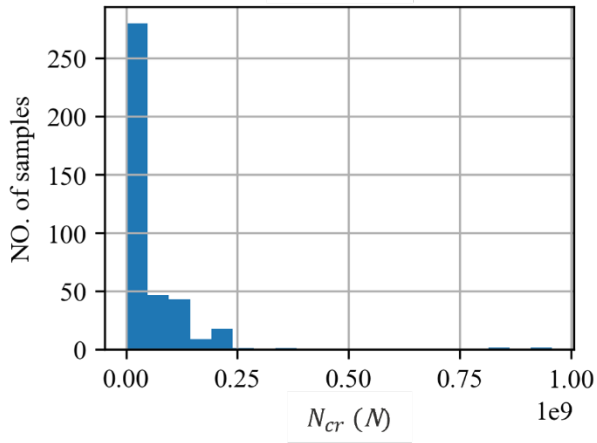
NO. of samples
N_{cr} (N)
1e9

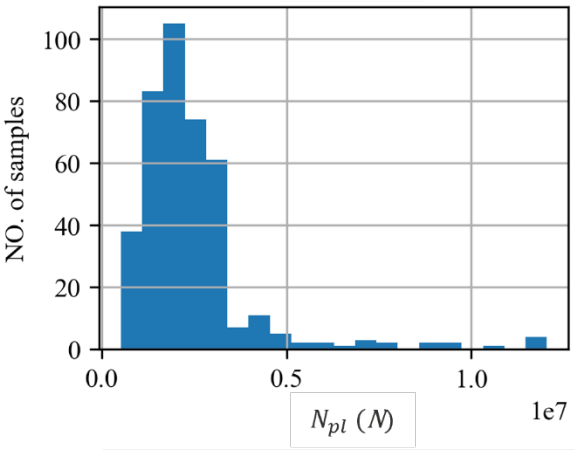
NO. of samples
N_{pl} (N)
1e7

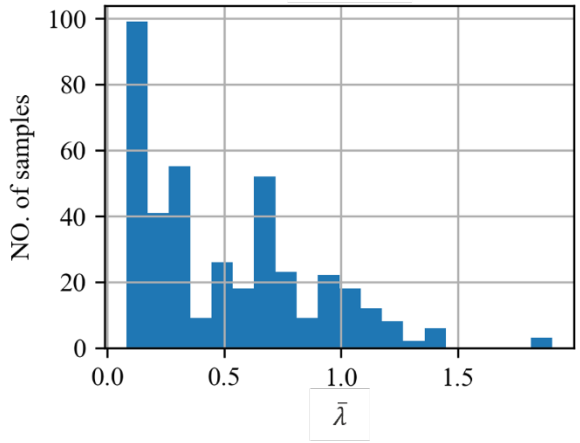
NO. of samples
$\bar{\lambda}$

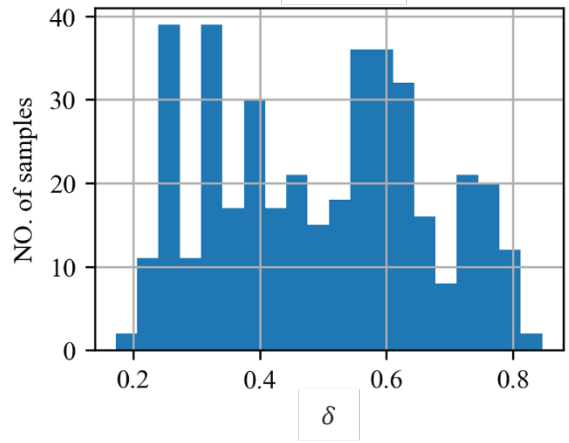
NO. of samples
δ

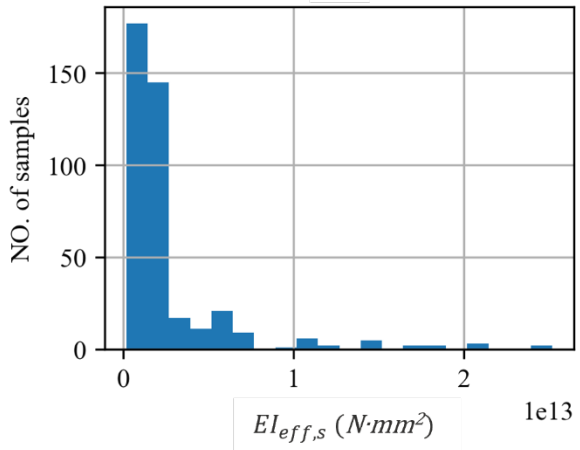
NO. of samples
$EI_{eff,s}$ (N·mm²)
1e13

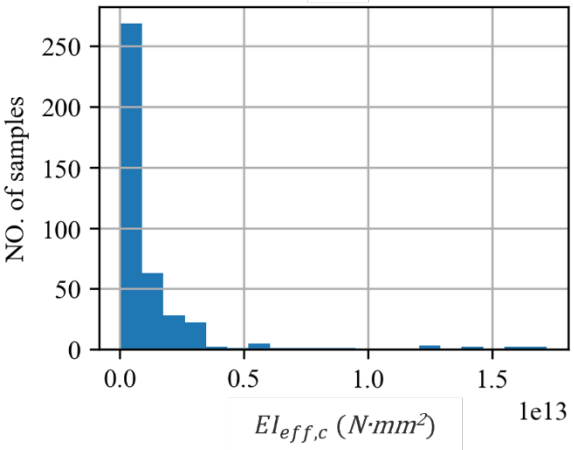
NO. of samples
$EI_{eff,c}$ (N·mm²)
1e13

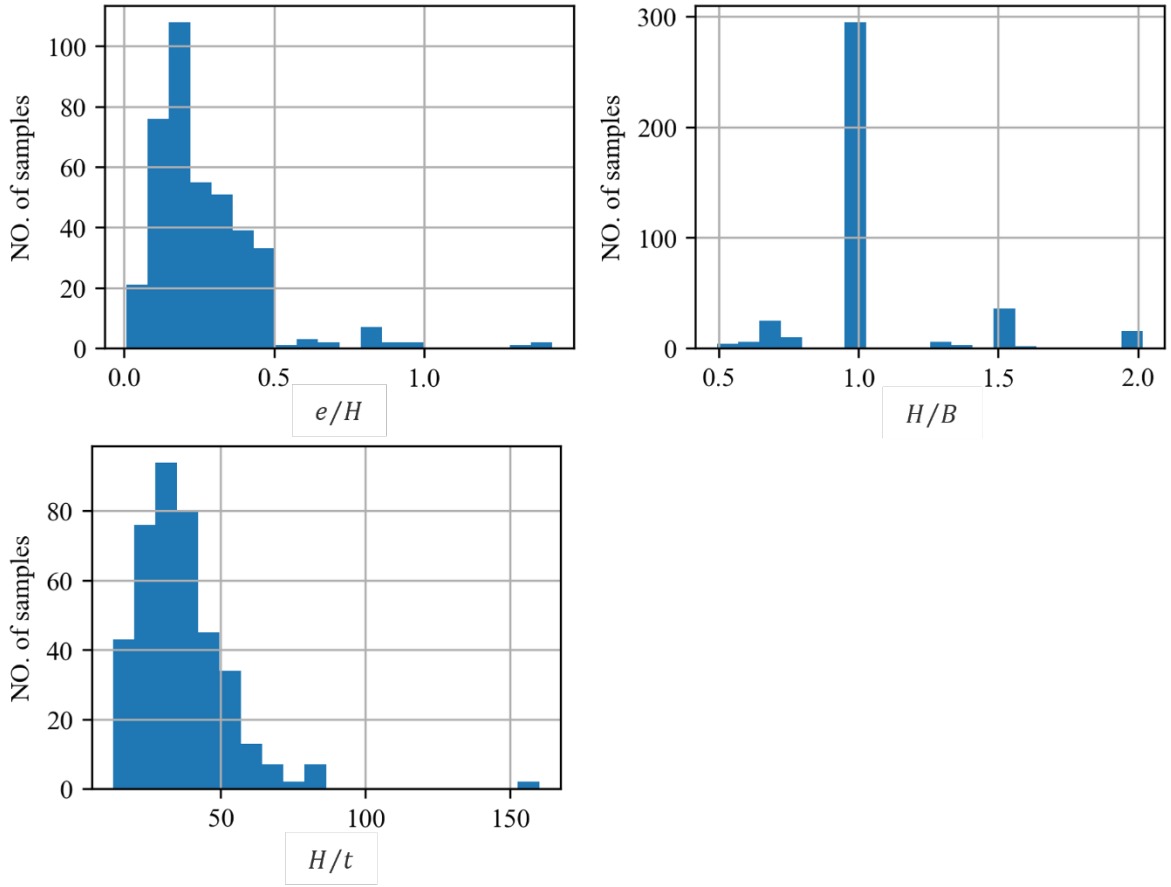

Figure 3 Statistical distribution of secondary features

The statistical analysis of individual input features for the database is helpful for the interpretation of the trained ML models in the following sections, because ML models learn from input data and the scarcity of training data in a certain range of an input feature may result in insufficient learning in that range. As such, the application of the trained ML model may be problematic in the range for which the model is not well trained.

2.2 Limitations of the established database

In addition to the fact that the database may result in insufficient training in some feature ranges as explained in the previous section, no distinction is made about the fabrication of steel tubes, either cold-formed, or welded, etc. Different fabrication processes may introduce different geometric imperfections, change of steel properties, and different residual stresses. Although distinction was not made about the fabrication process of steel tubes, the outer and inner corner radiuses were assumed in accordance with the specification in EN

10219-2 (CEN, 2006) if the steel tubes were explicitly mentioned to be cold-formed. Otherwise, the corners of the sections were assumed to be right angles. These assumptions will be used to calculate the geometric properties when using the design code methods but not for ML models.

Moreover, since the data were collected in different ages and regions, the potential systematic differences in terms of testing rigs, loading speed, measurement accuracies, etc., were not considered in the database. However, since the axial compressive strength is the focus, the influence of the above factors is believed to be mild.

3 Overview of machine learning methods

In this paper, three ML methods, Support Vector Regression (SVR), Random Forest Regression (RFR), and Neural Network (NN), are adopted. These three methods have been adopted and proved to be efficient in applications of structural engineering (Mangalathu & Jeon, 2019; Liu et al., 2021; Asteris et al., 2021). The three methods require limited numbers of hyperparameters when dealing with databases that consist of relatively limited data points. This feature is particularly favored by structural engineers, considering the fact that databases of structural engineering are usually small due to the high cost of structural tests.

3.1 Support Vector Regression (SVR)

Support vector machine (SVM) is extensively applied for classification and regression analyses using hyperplane classifiers. Linear SVR is illustrated in Figure 4. SVM was initially developed by Cortes & Vapnik (1995) for solving classification problems, and it was later extended for solving regression problems. SVM tries to minimize the upper bound on the expected risk based on the Structural Risk Minimization principle. Consider a regression problem using the linear SVR for a set of data, $\{(X_m, y_m), m = 1, \dots, n\}$, $X \in R^N$, $y \in R$, where n is the size of the database, X is the input, and y is the output. In this study, the output is the ultimate strength of CFSTs under eccentric loading. The aim is to find a hyperplane function that can estimate the

output value with good accuracy, $f(\boldsymbol{x}) = \boldsymbol{w} \cdot \boldsymbol{x} + b$, where $\boldsymbol{w}$ is a vector determining the orientation of the hyperplane, and b is the bias term.

The problem is expressed to minimize the empirical risk $R_{emp}(\boldsymbol{w}, b)$ as defined in Eq. 1, with the empirical risk of each sample in the database calculated by the error (ε)-insensitive loss function $L_\varepsilon(y, f(x))$ which is defined by Eq. 2.

$$R_{emp}(\boldsymbol{w}, b) = \frac{1}{n}\sum_{i=1}^{n} L_\varepsilon(y, f(x)) \tag{1}$$

$$L_\varepsilon(y, f(x)) = \begin{cases} \varepsilon, & x < 0 \\ |y_i - f(x_i)| - \varepsilon, & otherwise \end{cases} \tag{2}$$

The minimization in the empirical risk is equivalent to the convex optimization problem

$$min\left[\frac{1}{2}\boldsymbol{w} \cdot \boldsymbol{w} + C\left(\sum_{i=1}^{n} \xi_i + \sum_{i=1}^{n} \xi_i^*\right)\right] \tag{3}$$

$$\text{Subjected to } \begin{cases} y_i - w \cdot x_i - b \le \varepsilon + \xi_i \\ w \cdot x_i + b - y_i \le \varepsilon + \xi_i^* \\ \xi_i, \xi_i^* \ge 0 \end{cases} \tag{4}$$

where ξ_i and ξ_i^* are the slack variables introduced to allow a certain number of errors, C is the hyperparameter to control the tradeoff between the tolerance to errors and the flatness of the hyperplane. For nonlinear SVR regression problems, kernel functions are used to map the original input data into a higher-dimensional space (Platt, 1999; Amari & Wu, 1999). Essentially this is a technique of combining linear SVR and mapping input data into a higher-dimensional space. Various kernel functions, e.g., polynomial function, radial basis function, are available to transform the original input to different higher-dimensional space (Pedregosa et al., 2011).

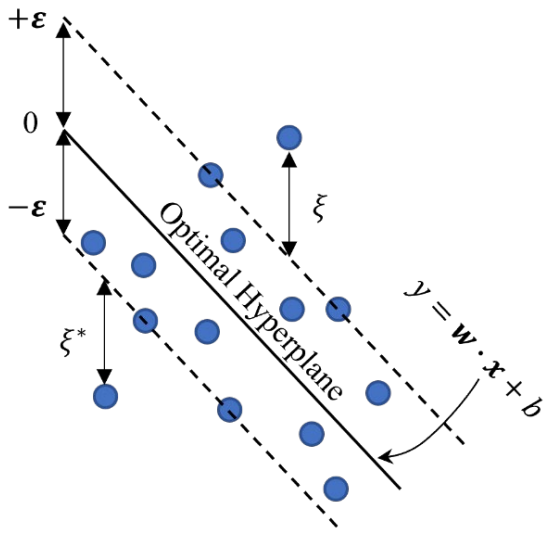

Figure 4 Illustration of linear support vector regression

3.2 Random Forest Regression (RFR)

A decision tree, also called classification or regression tree, is a statistical model firstly introduced by Breiman et al. (1984). Each decision tree is composed of decision nodes and leaf nodes, and grows during the training process. During the training process, the input data are split at each decision node based on the rule that will result in the lowest impurity in the split. There are various methods to quantify the impurity, for instance, the sum of the squared residuals, the mean squared residuals, etc. This process is repeated recursively until the prescribed stop criteria are met.

Random forest regression (RFR) is a method consisting of an ensemble of decision trees as shown in Figure 5. It takes advantage of two powerful techniques: bootstrap bagging and random feature selection (Breiman, 2001). In terms of bootstrap bagging, each tree is independently constructed using a database obtained through bootstrapping the training data with replacement. Moreover, during the training of each tree, instead of using all features, a randomly selected subset of the input features will be used to split the data at each decision node. For prediction, the mean value of the outputs of all the trees will be adopted (Breiman, 1996).

Unlike SVR which can process input variables to different forms through kernel functions, the decision trees do not process input variables and their growing is directly based on the fed input variables. As such, the

addition of some secondary input features that are more directly relevant to the output variable may be beneficial for the growing (data splits at the decision node) of decision trees. Moreover, because RFR uses the techniques of bootstrap sampling and random feature sampling, RFR models are generally not much affected by the multicollinearity among the input features (Dormann et al., 2013). In this study, four secondary features are selected through preliminary feature importance analysis and added as the input features for the training of the RFR model, namely, the steel section strength (A_sF_y), the concrete section strength (A_cf_c), the plastic strength of the whole section (N_{pl}), and the moment of inertia of the steel section (I_s).

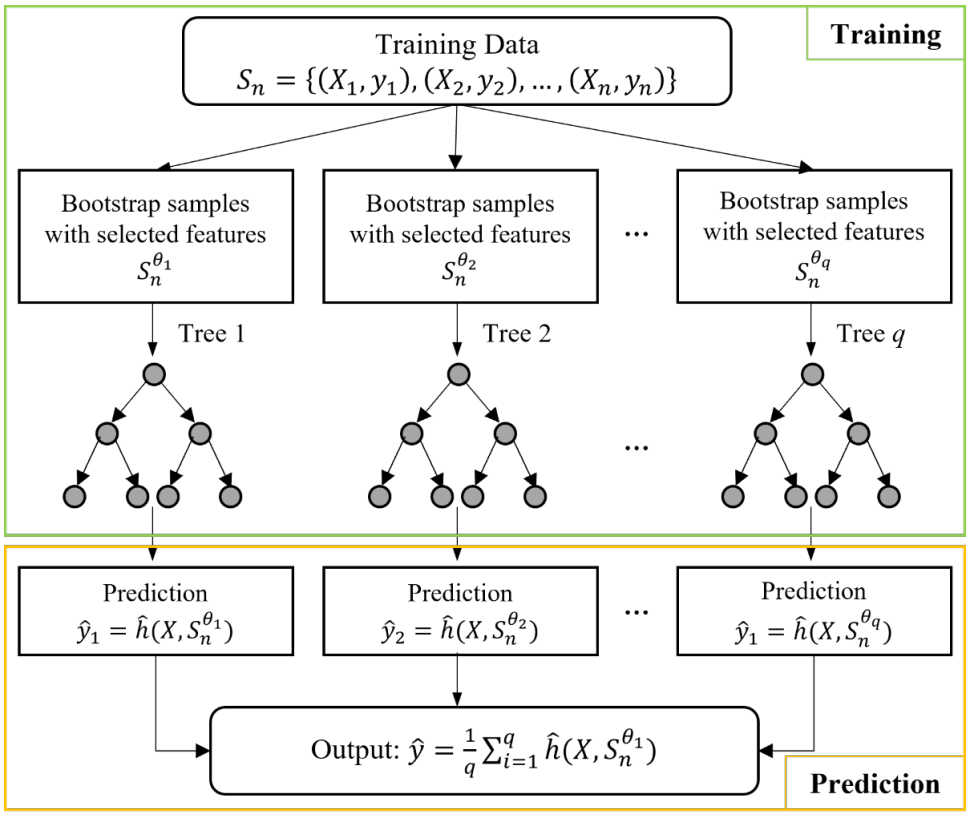

Figure 5 Illustration of random forest regression

3.3 Neural network (NN)

A neural network is a computational model inspired by biological neural networks (Fausett, 2006), that can adapt its predictions according to input data and make generalizations as illustrated in Figure 6. Among ML-based techniques, the NN is the prevailing method in civil engineering applications owing to its simplicity. A NN model consists of three types of layers of neurons (also called nodes), namely, the input, hidden and output

layers. The number of nodes in the input layers is equal to the number of input features, and the number of nodes in the output layer is equal to the number of output variables. For fully connected NN, each node in a layer is connected to all the nodes in the next layer. Each connection represents a relationship that is described mathematically by weight (w) and bias (b) parameters. The output of the node i in the hidden layer is

$$h_i = s\left(\sum_{j=1}^{N} w_{ij}x_j + b_{ij}\right) \quad (5)$$

where $s()$ is called the activation function, N is the number of input nodes. In this study, the *ReLU* function is used as the activation function. During training of a NN model, the weights and bias are optimized with the aim of minimizing the errors between true and predicted outputs (Hecht-Nielsen, 1992)

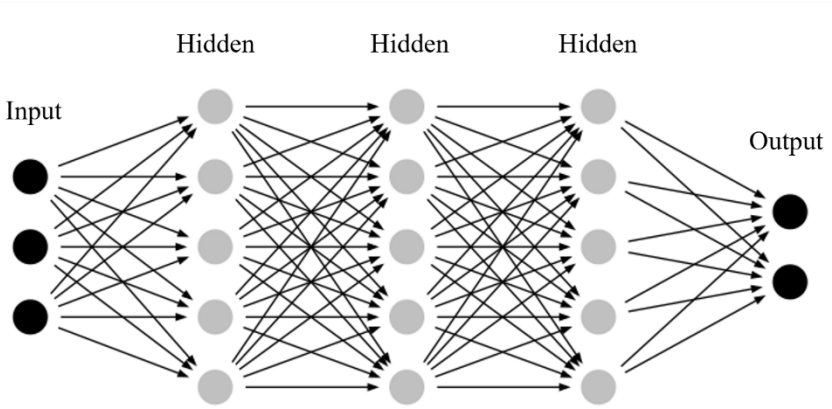

Figure 6 Illustration of neural network structure

4 Methods in design codes

For estimation of the ultimate compressive strength of CFSTs subjected to eccentricity, methods are available in some design codes. In this study, the methods in Eurocode EN 1994 (CEN, 2004) (referred to as the EU method) and AISC 360-16 (AISC, 2016) (referred to as the US method) are used to conduct the comparison with the ML models. The two methods have some limits on the applicability, as listed in Table 4, mainly due to the lack of experimental data outside the applicable range. As the values of geometric and material properties reported in the database were all measured, the safety factors were not included in the calculation so as to make the comparison more objective. A brief introduction about the methods in the codes is as follows.

Table 4 Limits on application of methods in design codes for CFST columns

Design code	F_y (MPa)	f_c (MPa)	Section slenderness	Extra
EN 1994	$235 \le F_y \le 460$	$25 \le f_c \le 50$	$H/t \le 52\sqrt{235/F_y}$	$0.2 \le A_s F_y / N_{pl} \le 0.9$ $\bar{\lambda} \le 2.0^{*}$
AISC 360-16	$F_y \le 525$	$21 \le f_c \le 69$	$H/t \le 5\sqrt{E_S/F_y}$	$A_s/A_{total} \ge 0.01^{**}$

[*] For simplified method

[**] A_{total} is the total area of the composite section

4.1 Eurocode EN 1994

Under concentric compressive loading, the squash load of rectangular CFST is calculated as

$$N_{pl} = A_s F_y + A_c f_c \tag{6}$$

To account for the possible global buckling, a reduction factor, χ, is introduced to calculate the ultimate compressive resistance,

$$N_u = \chi N_{pl}, \chi \le 1 \tag{7}$$

The estimation of χ is based on the relative slenderness of the column

$$\bar{\lambda} = \sqrt{N_{pl}/N_{cr}} \tag{8}$$

following Eurocode EN 1993 (CEN, 2005), with N_{cr} the critical buckling load whose calculation is based on the effective flexural stiffness $(EI)_{eff} = E_s I_s + 0.6 E_c I_c$.

Under pure bending, the flexural resistance (M_{pl}) of the CFST is determined assuming the stresses of the composite section at the ultimate limit state follow the distribution shown in Figure 7(b). Under the combined compression and uniaxial bending, an interaction curve as shown in Figure 7(a) is adopted. For convenience of calculation, a simplified curve, constructed based on four (*M*,*N*) pairs, is also provided. For eccentric compressive loading cased, the (*M*,*N*) response follows a straight line $M = N \cdot e$, the ultimate compressive strength can be taken as the *N* coordinate of the intersection point.

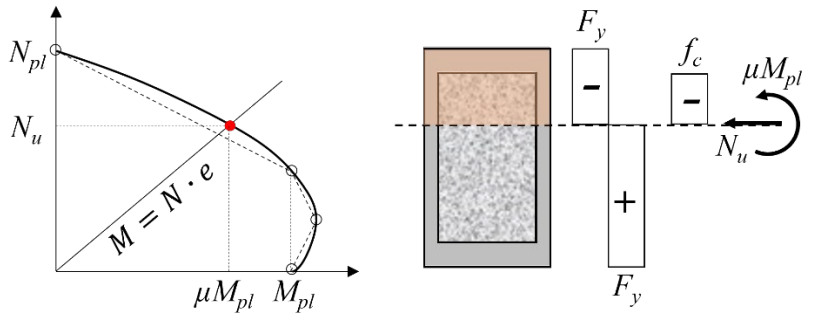

(a) (b)

Figure 7 (a) Compression-bending interactive curve; (b) Assumed stress distribution of the cross section

4.2 AISC 360-16

Under concentric compression, the resistance of a CFST is calculated as

$$P_n = \begin{cases} P_{no}(0.658^{P_{no}/P_e}), & P_{no}/P_e \le 2.25 \\ 0.877P_e, & P_{no}/P_e > 2.25 \end{cases} \quad (9)$$

where P_e is the elastic critical buckling resistance calculated based on the effective stiffness of the composite section $(EI)_{eff} = E_s I_s + C_1 E_c I_c$; P_{no} is the strength of the composite section, whose calculation is based on the slenderness ratio of the steel section to account for the local buckling. For compact sections, P_{no} is calculated as

$$P_{no} = A_s F_y + 0.85 A_c f_c \quad (10)$$

Under pure bending, the flexural strength is determined based on the categorization of the steel section

$$M_u = \begin{cases} M_p, & compact\ section \\ M_p - (M_p - M_y)\left(\dfrac{\lambda - \lambda_p}{\lambda_r - \lambda_p}\right), & noncompact\ section \\ M_{cr}, & slender\ section \end{cases} \quad (11)$$

M_p is the moment corresponding to plastic stress distribution over the whole composite cross section as shown in Figure 8(b); M_y is the yield moment corresponding to the yielding of the tension flange, first yielding of the compression flange, and linear stress distribution with maximum of 0.7fc of the compression concrete, as shown in Figure 8(c); M_{cr} is the first yield moment with the stress in the compression flange limited to the local buckling stress as shown in Figure 8(d).

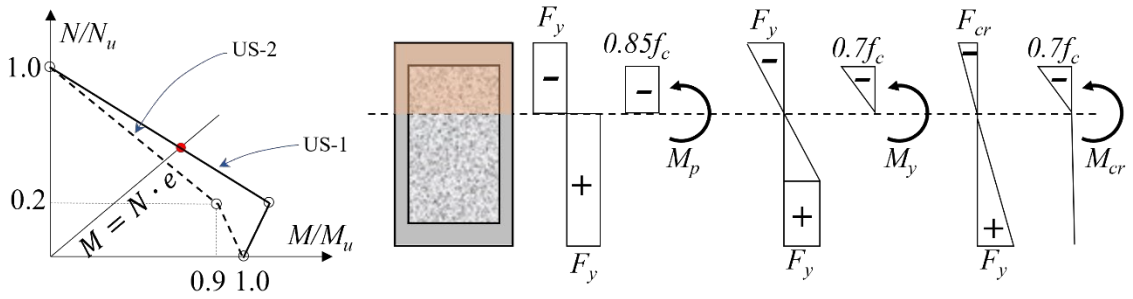

(a) (b) (c) (d)

Figure 8 (a) Compression-bending interactive curve; Stress distribution under (b) plastic moment, (c) yield moment, (d) critical moment

Under the combined bending and compression, two alternative *M*-*N* interaction curves are provided in AISC 360-16, as shown in Figure 8(a). The solid one, referred to as US-1 method, is described as

$$\begin{aligned} &\frac{P}{P_n}+\frac{1-c_p}{c_m}\frac{M}{M_u}=1, \qquad P/P_n \geq c_p \\ &\frac{1-c_m}{c_p}\frac{P}{P_n}+\frac{M}{M_u}=1, \qquad P/P_n < c_p \end{aligned} \tag{12}$$

where the coefficients, c_p, c_m, are calculated based on the steel to concrete strength ratio $c_{sr}=\frac{A_s F_y}{A_c f_c}$. The dashed one, referred to as US-2 method, follows the rule for general members and is described as

$$\begin{aligned} &\frac{P}{P_n}+\frac{8}{9}\frac{M}{M_u}\leq 1, \qquad P/P_n \geq 0.2 \\ &\frac{P}{2P_n}+\frac{M}{M_u}\leq 1, \qquad P/P_n < 0.2 \end{aligned} \tag{13}$$

Similarly, the *N* coordinate of the intersection point between the response line and the interactive curve is taken as the ultimate strength under eccentric loading.

5 ML training procedure

The database will go through a customized procedure for training of the three ML models, including train-test data split, feature scaling, hyperparameter tuning through cross validation. The optimization, training and evaluation of the ML models followed the procedure shown in Figure 9. Detailed explanation of each component of the whole procedure will be provided in this section. The open-sourced python-based ML package 'scikit-learn' was adopted in this study (Pedregosa et al., 2011).

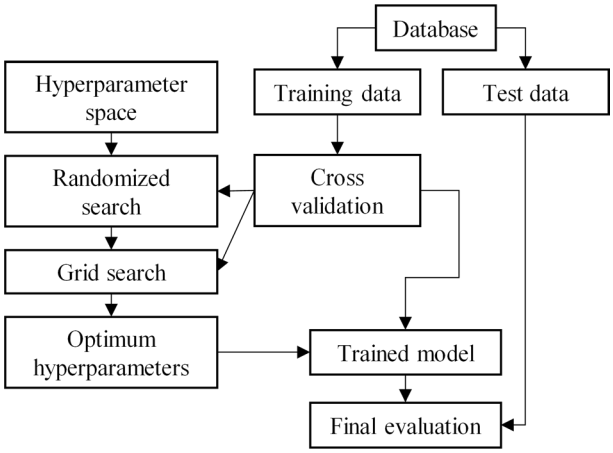

Figure 9 Optimization, training, and evaluation procedure for the ML models

5.1 Train-test data split

To evaluate the performance of the trained ML models on data that they have never seen, the 'train-test split' technique was adopted. The database is randomly shuffled first and then split to the training set (80% of the total data) and the test set (20% of the total data). Only the training set will be used for the optimization and training of the ML models, while the test set will be held out until the final evaluation of the models. It is worth noting that to facilitate fair and meaningful comparison of the predictive performance of the 3 ML models, the same training dataset will be used for training, and the same test dataset will be used for evaluating the predictive performance.

5.2 Feature selection

The correlation between all the 18 features (7 primary features and 11 secondary features) is shown in Figure 10. The correlation values between some features are high, which indicates there may be some information redundancy. Moreover, some of the features may be irrelevant to the ultimate strength of CFSTs. Inclusion of such features will reduce the efficiency of the ML models, and even mislead the ML models resulting in worse predictive performance. As such, a feature selection process was conducted to identify the most relevant features, which is elaborated as follows.

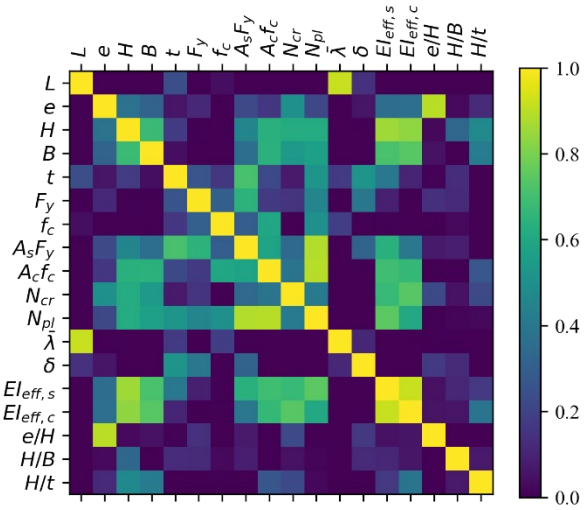

Figure 10 Correlation between both primary and secondary features

Firstly, all the 18 features were used to train the 3 ML models. Secondly, for each trained ML model, the importance values of individual features were calculated using the method of permutation feature importance. The permutation importance of a feature is defined as the decrease in a model performance score (R^2 in this study) when the feature is randomly shuffled (Breiman, 2001). By shuffling the feature, the relationship between the feature and the target is broken, and therefore the drop in the model score is indicative of how important the feature is. Thirdly, for each ML model, the importance values of all features are scaled by the same factor to have a sum of unity. Finally, the combined importance value of a feature is calculated by summing the importance values obtained from the 3 ML models, which is shown in Figure 11. For selection of features, a threshold of 5% is taken. In the end, 13 features that have the combined importance values above 5% were selected to train the 3 ML models.

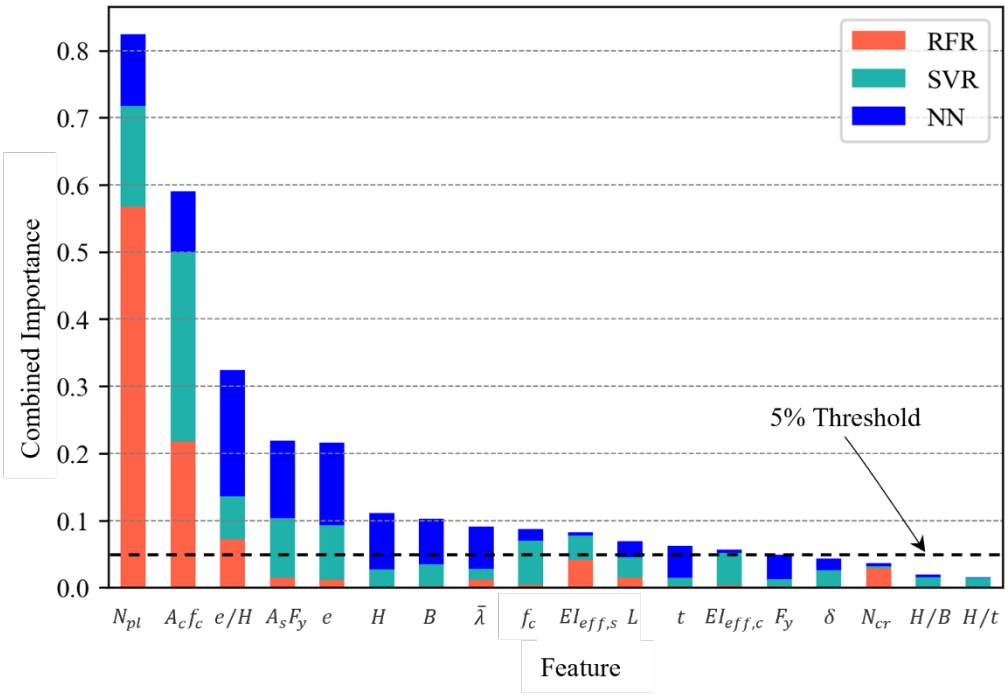

Figure 11 Feature selection based on combined feature importance

5.3 Feature scaling

Since different input features may have substantially different scales and the ranges of features vary widely, it is generally beneficial in ML algorithms to normalize the ranges of all input features so that each feature contributes approximately proportionately. Moreover, ML methods using gradient descent usually converge faster with feature scaling than without it. In this study, as each feature does not follow a specific distribution, all features were scaled to the range [0,1] before being fed to the ML models. To avoid that information outside the training set is used to create the model (also known as data leakage), a Pipeline object is created, in which only the training data will be used to create the scaler that will be used to scale the features.

5.4 Hyperparameter optimization strategy

Hyperparameters of a ML model are parameters that control the learning process, and they have to be tuned so that the model can optimally solve the problem. Hyperparameter optimization finds a tuple of hyperparameters that yields an optimal model which minimizes a predefined loss function on given data (Claesen & De Moor, 2015).

To estimate the generalization performance of the model, five-fold cross validation was used. As shown in

Figure 12, the training data was further split into five folds. The model is trained using four folds of data, and the left fold is used as the validation set. This process was repeated five times, with each time using a different fold as the validation set. The performance of the model for each of the five iterations is then averaged to produce an overall measurement.

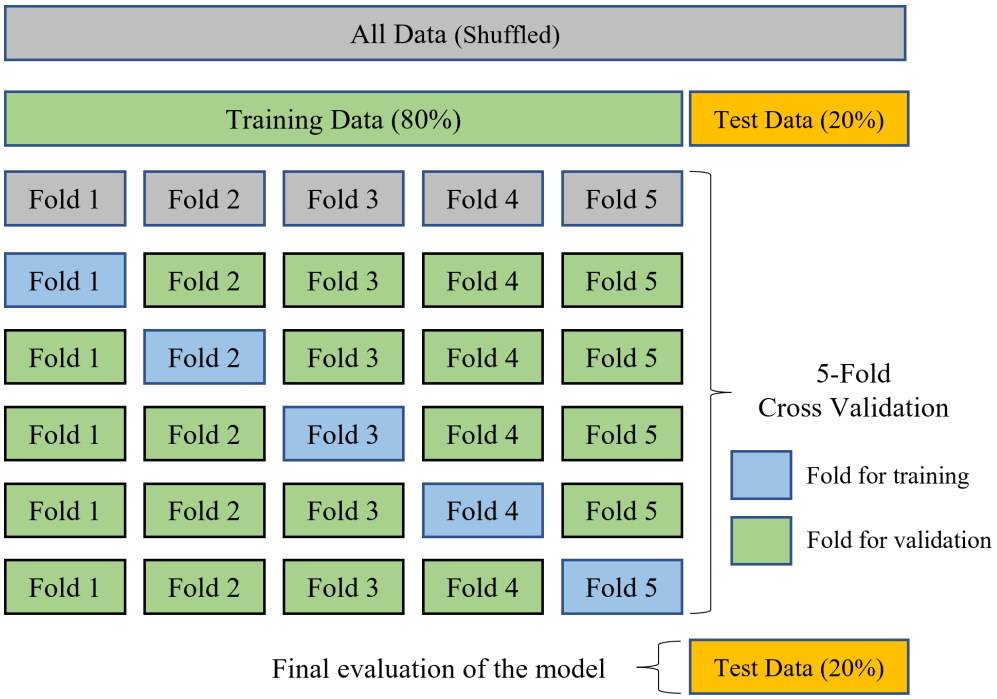

Figure 12 Five-fold cross validation adopted in this study

A two-step hyperparameter optimization strategy was adopted in this study. Firstly, for each hyperparameter (either numerical or categorical), values that cover a wider range were selected. Therefore, a large space was created for the hyperparameter combination. Random search was conducted through the RandomizedSearchCV method in which value was randomly selected for each hyperparameter and evaluated. Based on the prescribed performance metric, the hyperparameters were preliminarily optimized.

In the second step, for each hyperparameter, values covering a smaller range around the preliminarily optimized value obtained in the first step were selected. In this way, a relatively smaller hyperparameter space was created. The grid search was conducted using the GridSearchCV method, which is an exhaustive searching through the whole defined space. Figure 13 illustrates the effect of two hyperparameters on the R^2 scoring

obtained through the five-fold cross validation for each of the 3 ML models. The hyperparameter that yields the highest R^2 scoring will be taken as the optimal one.

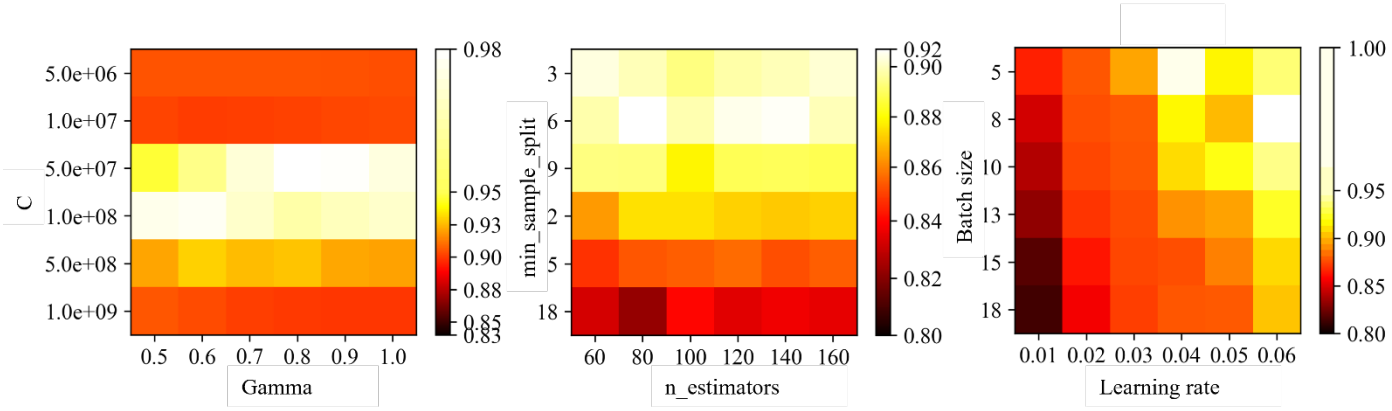

(a) (b) (c)

Figure 13 Effect of two hyperparameters on the R^2 scoring of the ML model: (a) SVR, (b) RFR, (c) NN

To avoid the possible overfitting, in which the ML model performs well on the training data but fails to generalize and perform well on unseen data, the hyperparameter searching process was closely monitored during the cross validation to ensure that the performance on the validation fold was close to that on the training fold. It is noted that for the NN model, although increasing the number of hidden layers and the number of neurons in each layer may result in improved performance in some cases, the optimization process will be stopped if the performance improvement is less than 1% in terms of the performance metric R^2. The obtained optimized hyperparameter values for the three ML models are listed in Table 5.

Table 5 Optimal hyperparameters adopted for the SVR, RFR, NN models

ML model	Hyperparameters
SVR	*Gamma*=0.8, *C*=5e7, *kernel function*='rbf'
RFR	*n_ estimators*=80, *max_depth*=40, *min_sample_split*=6, *min_sample_leaf*=3, *max_features*='auto'
NN	*Number of hidden layers*=2, *nodes of hidden layers*=(40,40), *learning_rate*=0.06, *batch_size*=8

6 Model performance evaluation

6.1 Performance metrics

Various performance metrics are available to evaluate the performance of ML models. Five popular ones are

adopted in this study, namely, the mean ratio (MR), the mean absolute percentage error (MAPE), the coefficient of determination (also known as the R squared value, R^2), the a20 index, and the mean absolute error (MAE). Their mathematical calculation follows the Eqs. 14-18, where n is the number of data points, y_{pi} is the predicted value, and y_i is the true value.

$$MR = \frac{1}{n}\sum_{i=1}^{n}\frac{y_{pi}}{y_i} \tag{14}$$

$$R^2 = 1 - \frac{\sum_{i=1}^{n}\left(y_i - y_{pi}\right)^2}{\sum_{i=1}^{n}\left(y_i - \frac{1}{n}\sum_{j=1}^{n} y_j\right)^2} \tag{15}$$

$$MAPE = \frac{1}{n}\sum_{i=1}^{n}\left|\frac{y_i - y_{pi}}{y_i}\right| \tag{16}$$

$$RMSE = \sqrt{\frac{1}{n}\sum_{i=1}^{n}\left(y_i - y_{pi}\right)^2} \tag{17}$$

$$a20 = \frac{n_{20}}{n}, n_{20}\ is\ the\ number\ of\ samples\ with\ 0.8 \le \frac{y_{pi}}{y_i} \le 1.2 \tag{18}$$

6.2 Comparison of ML models with design code methods

In Figure 14, the comparison between the predicted strengths and the corresponding experimentally obtained strengths are plotted for both the ML models and code methods. A 45-degree dashed line is provided in each plot. The closer to the dashed line, the prediction is more accurate. Moreover, the performance of each model/method was evaluated by the metrics mentioned in the previous section, whose values are listed in Table 6.

The ML models outperformed the code methods from the perspective of all the studied performance metrics. The points of ML models are distributed closer to the 45-degree dashed line that those of the code methods. The MRs of code methods are all below 1.0, representing conservative predictions, while the values of MRs are around 1.0 for the ML models, representing more accurate predictions. This is reasonable as design codes are inclined to be conservative to yield safer designs.

In terms of the mean absolute percentage error, the values of ML models are all below 0.15, while those of

code methods are all above 0.15. Regarding the R^2 which measures the proportion of total variance of outcomes explained by the model, all the three ML models achieved a value above 0.95, while the code methods yielded values below 0.88. A method is generally considered to have good accuracy when R^2 is above 92% and MAPE is less than 15% (Prayogo et al., 2020; Olalusi & Awoyera, 2021; Abuodeh et al., 2020; Zhang et al., 2020). Therefore, all the three ML methods can be evaluated to be good models.

Table 6 Summary of calculated performance metrics for ML models and code methods

Model	Database	MR	MAPE	R2	a20	RMSE (*N*)
EU	All	0.90	0.15	0.88	76%	337755
US-1	All	0.84	0.20	0.85	49%	379834
US-2	All	0.78	0.25	0.78	41%	469862
SVR	Training	1.01	0.04	0.99	98%	74386
	Test	1.01	0.08	0.97	90%	143907
	All	1.01	0.05	0.99	96%	92647
RFR	Training	1.03	0.08	0.97	93%	175097
	Test	1.06	0.13	0.93	84%	228953
	All	1.03	0.09	0.96	91%	187170
NN	Training	1.02	0.11	0.97	86%	170113
	Test	1.04	0.13	0.96	84%	174585
	All	1.03	0.12	0.97	86%	171021

The a20 index evaluates the portion of predictions that are within the ±20% margin of error compared with the experimental values. The three ML models exhibited a20 indexes of greater than 84% while the code methods showed a20 indexes of smaller than 76%. A higher portion of predictions within a certain error margin is beneficial for structural design as it will result in lower resistance reduction to achieve a certain level of safety. Similar performance improvement can be found for the ML models from the perspective of RMSE.

Among the three ML models, similar performance was achieved in terms of R^2 and MR. The SVR model outperformed the RFR and NN models based on the MAPE and a20 index for the test dataset. The lowest MAPE value (0.08) was achieved by the SVR model, while the values were 0.13 (63% higher) for both the RFR and NN models. Moreover, the SVR model showed the highest a20 index (90%) for the test dataset,

while the values were 84% for both the RFR and NN models.

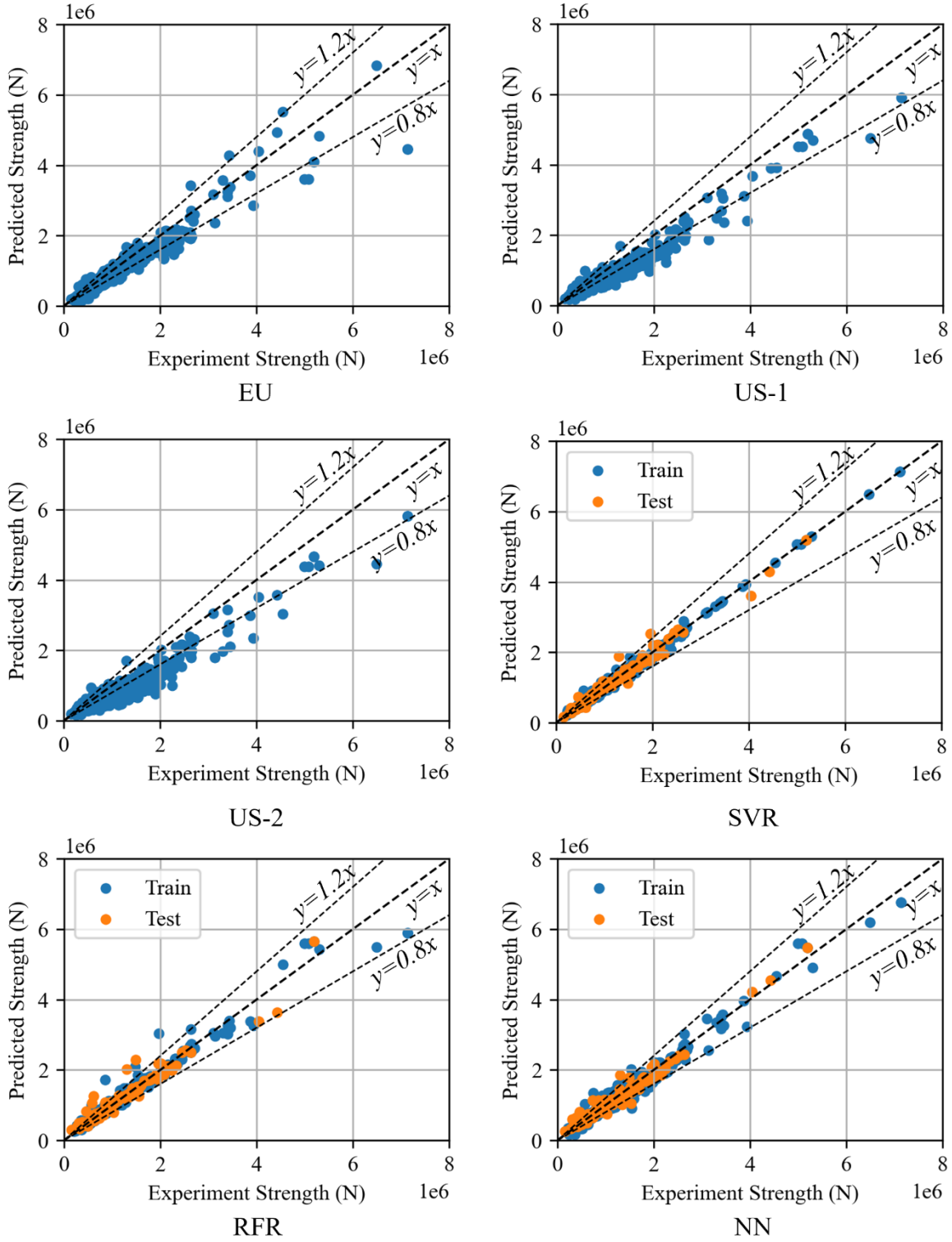

Figure 14 Comparison between predicted strength and experimental strength

7 Parametric study

ML models can be understood as approximating a target function that maps input variables to an output variable. Although the relationships between the inputs and output in ML models are not as explicit as in a mathematical formula, they can be interpreted through parametric studies in which only the input feature of

interest is varied. In this study, the parametric study was conducted for all the primary input features using the ML models and the code methods. As the US-1 method is based on the compression-bending interactive curve specific for composite sections while the US-2 method is based on the curve for general sections, only the US-1 method is considered in the parametric study. For the parametric study of each feature, experimental samples (if available) will be used as the reference to evaluate the behavior of different models. The results of the parametric studies are presented in Figure 15.

7.1 Effect of eccentricity

Four specimens were reported in Matsui & Tsuda (1996) of which the only varying parameter was the loading eccentricity. As shown in Figure 15(a), the experimental data points reveal, as anticipated, a trend that: with the increase of eccentricity, the ultimate strength decreased; the slope is steep initially but diminishes with increase of eccentricity. This is reasonable because with the increase of e, the failure of the composite section will be shifted from being compression-dominated to bending-dominated. Under the compression-dominated situation, both the steel tubes and the concrete core will contribute to resist the load. In contrast, under the bending-dominated loading, the concrete on the tension side will generally not contribute to resist the load and the neutral axis of the section will be shifted to the compression side. The net compression resistance of the whole section will therefore diminish.

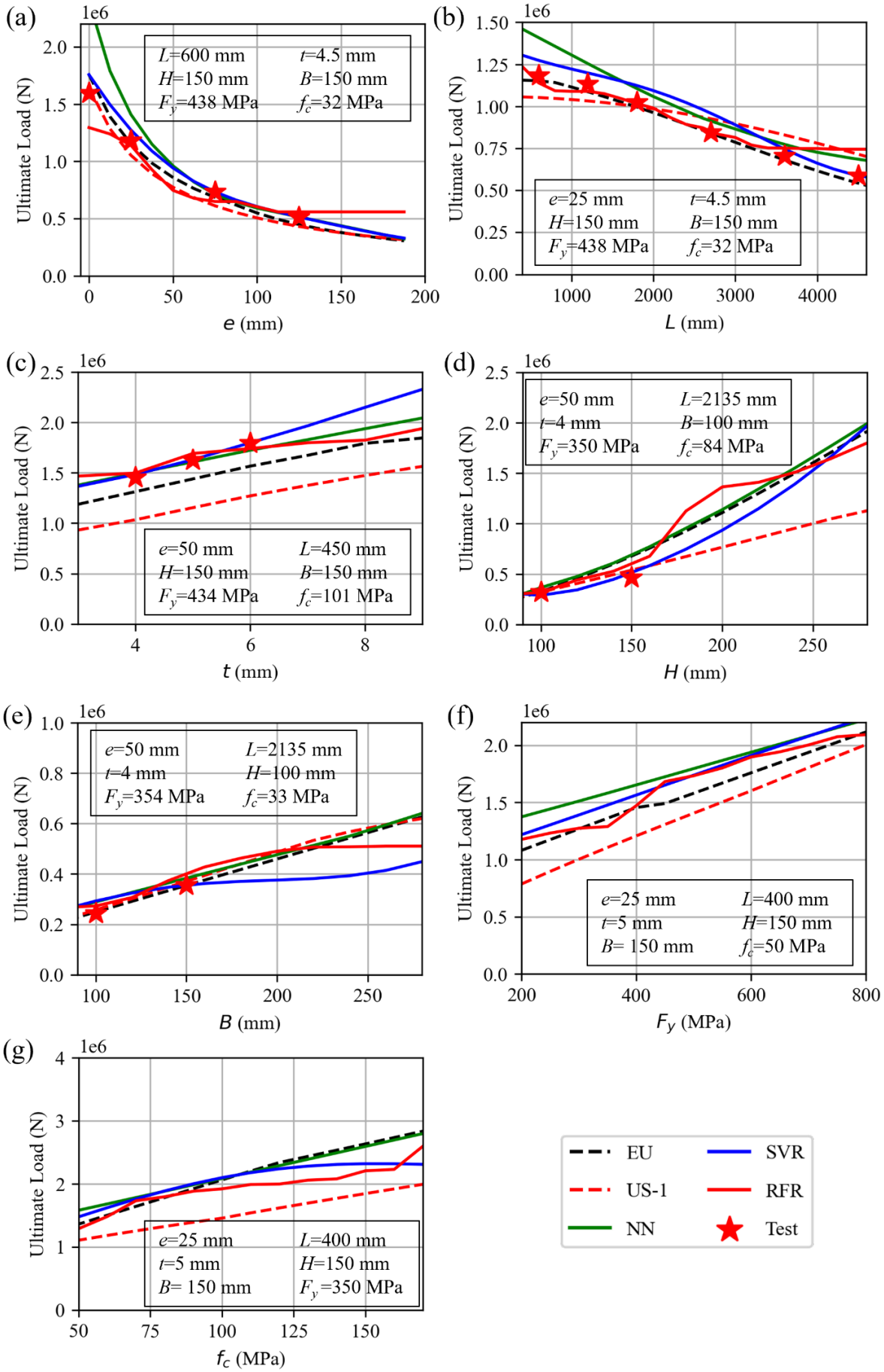

Figure 15 Parametric study (a) e [test data from Matsui & Tsuda (1996)]; (b) L [test data from Matsui & Tsuda (1996)]; (c) t [test data from Li et al. (2018)]; (d) H [test data from Hernández et al. (2012a)]; (e) B [test data from Hernández et al. (2012b)]; (f) F_y; (g) f_c

All the three ML models and the two code methods captured the trend indicated by the experimental data. For the four experimental tests, all the models/methods except the NN model predicted the ultimate strength with good accuracy and behaved almost the same with e up to 125 mm. Although the NN model captured the general trend, it seemed to have simplified the relationship to be bilinear. This inaccuracy of the NN model may be attributed to the insufficient training over the studied range of e. As shown in Figure 2, e of the training data concentrated in the range of 1-70 mm.

7.2 Effect of column length

Experimental tests were conducted by Matsui & Tsuda (1996) to study the effect of column length on the ultimate strength of CFSTs under eccentric loading. The results of six specimens, of which the only varying parameter was the column length, were presented in Figure 15(b). The lengths of the six specimens ranged from 600 mm to 4500 mm. As shown the six experimental data points indicated a trend that the ultimate strength decreases with the increase of the column length. The strength decrease rate is slow at small values of L and gradually increases with the increase of L. This trend agrees well with the buckling curve of a general column. When the column length is small (i.e., short column), the strength of the column will be determined by its section, as global buckling will not occur. In this case, the strength of the column will not be much affected by the column length. With the increase of column length, the failure may shift to global buckling. Column length in this case will play a key role: the longer the column is, the slender the column will be, and the lower buckling strength will be obtained.

All the ML models and the code methods captured the general relationship between column length and the ultimate strength. The EU method and the SVR model provided the best fit to the experimental data points. The RFR model matched well with the trend with L up to 3500 mm, but then deviated from the trend with a sudden change in the slope. Similarly, the NN model performed well with L up to 3000 mm, after which the

418 curve deviated from the trend with a smaller slope. The inaccuracy of both the RFR and NN models for long
419 columns is believed to be attributed to the scarcity of training data in this range. As shown in Figures 2 and 4,
420 the lengths of most data lie in the range of 500-3000 mm, and most data have the value of $\bar{\lambda}$ below 1.0
421 indicating short columns without global buckling.

422 **7.3 Effect of cross-section dimensions**

423 Figures 15(c)-(e) present the results of the parametric study on the three primary cross-section dimensions, *H*,
424 *B*, and *t*. For the effect of *t*, the three experimental data points indicated a positive linear trend. Generally, this
425 positive linear trend was captured by all the ML models and code methods. But the three ML models yielded
426 more accurate predictions for the experimental data points, while the code methods made conservative
427 predictions, especially the US-1 method.

428 For the effect of *H*, the five models/methods predicted different trends although they all yielded good
429 predictions for the two experimental data points. Both the EU and US-1 methods made a positive linear
430 prediction but with different slopes. A nonlinear relationship with increasing slope was made by the SVR
431 model. A similar trend was predicted by the NN model but with a simplified bilinear relation. The RFR model
432 predicted a general linearly increasing trend with oscillations. More experimental tests with *H* greater than
433 150 mm are needed to validate the various trends predicted by the different models/methods.

434 With regards to varying *B*, almost the same positive linear curve was made by all the models/methods, except
435 that the SVR model predicted a curve which increased with *B* up to 150 mm and then decreased. With *B*=150
436 mm, the width-to-thickness ratio of the compression flange in this case is below 40, which is smaller than the
437 critical local buckling limits specified in both Eurocode EN 1994 (CEN, 2004) and AISC 360-16 (AISC, 2016)
438 by a fair amount of margin. No local buckling is believed to occur, and the strength is therefore not expected
439 to decrease. As such, the SVR model is not deemed reliable in this case when *B* is more than 150 mm.

7.4 Effect of material strengths

Due to the absence of relevant experimental tests of which only the material strengths were varied, the effect of material strengths was studied only based on the ML models and code methods. When F_y is the studied parameter, a range of 200 to 800 MPa was covered; when the effect of f_c is studied, a range of 30 to 180 MPa was covered. As shown in Figure 15(f), a positive linear relationship with similar slope was generally predicted between F_y and the ultimate strength, except that the RFR curve featured some oscillation. In terms of the effect of f_c, the NN model, the EU and US-1 methods predicted a positive linear relationship over the studied range. The RFR curve is characterized by a trilinear relationship. Except for the US-1 method, all the other four models/methods predicted similar relationship between f_c and the ultimate strength for f_c up to 100 MPa, beyond which the ML models may not be reliable as training data in this range are scarce.

Conclusions

In this study, three ML methods were adopted to predict the ultimate strength of CFSTs under eccentric loading. A database of 403 experimental tests was created from literature. The database was then split to a training set which was used to optimize and train the ML models, and a test set which was used to evaluate performance of trained ML models. The performance of ML models was compared with that of methods in two typical design codes. Parametric analyses about the effect of each input feature on the ultimate strength were conducted using the ML models and code methods. The major conclusions are as follows:

1. Statistical analysis of the collected database reveals that, in terms of material strengths, a wide range was covered, but the data distribution was not even over the range. The sections of most specimens were small to medium sized and were subjected to low to moderate eccentricity.

2. The three ML models outperformed the code methods from the perspective of five typical performance metrics. Notably, mean ratios (MRs) of around 1.0 were achieved by the three ML models, while the

MRs were below 1.0 for the code methods representing conservative predictions. In terms of the a20 index which is the portion of predictions that are within the ±20% margin of error, the three ML models exhibited a20 indexes of greater than 80% while the code methods showed a20 indexes of smaller than 76%.

3. Among the three ML models, the lowest MAPE value (0.08) was achieved by the SVR model, while the value was 0.13 (63% higher) for both the RFR and NN models. Moreover, the SVR model showed the highest a20 index (90%) for the test dataset, while the values were 84% for both the RFR and NN models.

4. The parametric study revealed that the trained ML models could generally capture the effect of each primary input feature, which was verified by the relevant experimental test results.

However, although the ML models achieved notable improvement in prediction accuracy as compared with the code methods, their interpretation and application need caution when the input features are in the range where training data are scarce. Experimental studies are needed to expand the database in the range where data are relatively less.

Data

The database and the trained ML models will be available from the corresponding author on request.

Acknowledgement

The research work presented in this paper was supported by the Chinese National Engineering Research Centre for Steel Construction (Hong Kong Branch) and the Seed Funding from the Department of Civil and Environmental Engineering at The Hong Kong Polytechnic University.

Reference

Abuodeh, O. R., Abdalla, J. A., & Hawileh, R. A. (2020). Prediction of shear strength and behavior of RC beams strengthened with externally bonded FRP sheets using machine learning techniques. Composite Structures, 234, 111698.

AISC. (2016). Specification for structural steel buildings ANSI/AISC 360-16. American Institute of Steel Construction: Chicago, USA.

Amari, S. I., & Wu, S. (1999). Improving support vector machine classifiers by modifying kernel functions. Neural Networks, 12(6), 783-789.

Asteris, P. G., Lemonis, M. E., Le, T. T., & Tsavdaridis, K. D. (2021). Evaluation of the ultimate eccentric load of rectangular CFSTs using advanced neural network modeling. Engineering Structures, 248, 113297.

Breiman, L. (1996). Bagging predictors. Machine learning, 24(2), 123-140.

Breiman, L. (2001). Random forests. Machine learning, 45(1), 5-32.

Breiman, L., Friedman, J. H., Olshen, R. A., & Stone, C. J. (1984). Classification and regression trees. Belmont, CA: Wadsworth. International Group, 432(151-166), 9.

Bridge, R. Q. (1976). Concrete Filled Steel Tubular Columns. Research Report No. R283, School of Civil Engineering, University of Sydney, Sydney, Australia.

Cai, J. and He, Z.-Q. (2007). Eccentric-loaded behavior of square CFT columns with binding bars. Journal of Building Structures, 28(4), 25-35. (in Chinese)

Cederwall, K., Engstrom, B., and Grauers, M. (1991). High-Strength Concrete Used in Composite Columns. ACI SP 121-11: Second International Symposium on Utilization of High-Strength Concrete, Berkeley, CA, 195–214.

CEN. (2004). EN1994-1: Design of composite steel and concrete structures - Part 1-1: General Rules and Rules for Buildings. Brussels, Belgium.

CEN. (2005). EN1993-1: Design of steel structures - Part 1-1: General Rules and Rules for Buildings. Brussels, Belgium.

CEN. (2006). EN 10219-2: Cold formed welded structural hollow sections of non-alloy and fine grain steels - part 2: tolerances, dimensions, and sectional properties. European Committee for Standardization, Brussels, Belgium.

Chen, J., Chan, T. M., & Chung, K. F. (2021). Design of square and rectangular CFST cross-sectional capacities in compression. Journal of Constructional Steel Research, 176, 106419.

Chen, Y., Zhang, Y. C., and Dong, Z. J. (2005). Experimental Study of Static Behavior for Square Long Columns with Different Cross-Sections of Concrete-filled Thin-walled Steel Tube. Journal of Harbin Instlitute of Technology, 37(Sup.), 108-122. (in Chinese)

Claesen, M., & De Moor, B. (2015). Hyperparameter search in machine learning. arXiv preprint arXiv:1502.02127.

Cortes, C., & Vapnik, V. (1995). Support-vector networks. Machine learning, 20(3), 273-297.

Dormann, C. F., Elith, J., Bacher, S., Buchmann, C., Carl, G., Carré, G., ... & Lautenbach, S. (2013). Collinearity: a review of methods to deal with it and a simulation study evaluating their performance. Ecography, 36(1), 27-46.

Du, Y., Chen, Z., Wang, Y.-B., and Liew, J. Y. R. (2017). "Ultimate resistance behavior of rectangular concrete-filled tubular beam-columns made of high-strength steel." Journal of Constructional Steel Research, 133, 418–433.

Du, Y., Chen, Z., Zhang, C., & Cao, X. (2017). Research on axial bearing capacity of rectangular concrete-filled steel tubular columns based on artificial neural networks. Frontiers of Computer Science, 11(5), 863-873.

Fausett, L. V. (2006). Fundamentals of neural networks: architectures, algorithms and applications. Pearson Education.

Fujimoto, T., Mukai, A., Nishiyama, I., and Sakino, K. (2004). Behavior of Eccentrically Loaded Concrete-Filled Steel Tubular Columns. Journal of Structural Engineering, 130(2), 203.

Grauers, M. (1993). Composite Columns of Hollow Steel Sections Filled with High Strength Concrete. Ph.D. Dissertation, Chalmers University, Göteborg, Sweden.

Guo, L. H. (2006). Theoretical and experimental research on the behavior of concrete-filled rectangular hollow section steel tubes. Ph.D. Dissertation, Harbin Institute of Technology, Harbin, China. (in Chinese)

Guo, L. H., Zhang, S. M., and Tian, H. (2004). High strength concrete-filled RHS steel tubes subjected to eccentric

loading. Journal of Harbin Institute of Technology, 36(3), 297-301. (in Chinese)
Guo, L. H., Zhang, S. M., Wang, Y. Y., and Liu, J. P. (2005). Experimental and analytical research on axially load slender high strength concrete-filled RHS tubes. Industrial construction, 35(3), 75-79. (in Chinese)
Han, L. H. and Yao, G. H. (2003). Influence of concrete compaction on the strength of concrete-filled steel RHS columns. Journal of Constructional Steel Research, 59(6), 751–767.
Han, L. H. and Yao, G. H. (2004). Experimental Behaviour of Thin-Walled Hollow Structural Steel (HSS) Columns Filled with Self-Consolidating Concrete (SCC). Thin-Walled Structures, 42(9), 1357–1377.
Han, L.-H., Zhao, X.-L., and Tao, Z. (2001). Tests and mechanics model for concrete-filled SHS stub columns, columns and beam-columns. Steel and Composite Structures, 1(1), 51-74.
Hecht-Nielsen, R. (1992). Theory of the backpropagation neural network. In Neural networks for perception (pp. 65-93). Academic Press.
Hernández-Figueirido, D., Romero, M. L., Bonet, J. L., and Montalvá, J. M. (2012a). Influence of Slenderness on High-Strength Rectangular Concrete-Filled Tubular Columns with Axial Load and Nonconstant Bending Moment. Journal of Structural Engineering, 138(12), 1436–1445.
Hernández-Figueirido, D., Romero, M. L., Bonet, J. L., and Montalvá, J. M. (2012b). Ultimate capacity of rectangular concrete-filled steel tubular columns under unequal load eccentricities. Journal of Constructional Steel Research, 68(1), 107–117.
Huang, H., Chen, M. C., and Wan, C. Y. (2011). Behavior of concrete-filled stiffened square steel tubes subjected to eccentric compressive load. China Civil Engineering Journal, 44(10), 26–34. (in Chinese)
Huang, Z., Uy, B., Li, D., and Wang, J. (2020). "Behaviour and design of ultra-high-strength CFST members subjected to compression and bending." Journal of Constructional Steel Research, 175, 106351.
Jayalekshmi, S., Jegadesh, J. S., & Goel, A. (2018). Empirical approach for determining axial strength of circular concrete filled steel tubular columns. Journal of The Institution of Engineers (India): Series A, 99(2), 257-268.
Knowles, R. B. and Park, R. (1969). Strength of Concrete Filled Steel Tubular Columns. Journal of the Structural Division, ASCE, 95(12), 2565-2587.
Le, T. T., Asteris, P. G., & Lemonis, M. E. (2021). Prediction of axial load capacity of rectangular concrete-filled steel tube columns using machine learning techniques. Engineering with Computers, 1-34.
Lee, H.-J., Choi, I.-R., and Park, H.-G. (2017). "Eccentric Compression Strength of Rectangular Concrete-Filled Tubular Columns Using High-Strength Steel Thin Plates." Journal of Structural Engineering, 143(5), 04016228.
Li, G., Chen, B., Yang, Z., & Feng, Y. (2018). Experimental and numerical behaviour of eccentrically loaded high strength concrete filled high strength square steel tube stub columns. Thin-Walled Structures, 127, 483-499.
Li, G.-C., Chen, B.-W., Yang, Z.-J., Liu, Y.-P. and Feng, Y.-H.(2021). "Experimental and numerical behavior of eccentrically loaded square concrete-filled steel tubular long columns made of high-strength steel and concrete." Thin-Walled Structures, 159: 107289.
Liew, J. R., Xiong, M., & Xiong, D. (2016). Design of concrete filled tubular beam-columns with high strength steel and concrete. Structures. Vol. 8, pp. 213-226. Elsevier.
Liu, D. (2004). Behaviour of high strength rectangular concrete-filled steel hollow section columns under eccentric loading. Thin-walled structures, 42(12), 1631-1644.
Liu, D. (2006). Behaviour of eccentrically loaded high-strength rectangular concrete-filled steel tubular columns. Journal of Constructional Steel Research, 62(8), 839-846.
Liu, T., Wang, Z., Zeng, J., & Wang, J. (2021). Machine-learning-based models to predict shear transfer strength of concrete joints. Engineering Structures, 249, 113253.

Long, Y.-L. and Cai, J. (2008). Eccentric Compressive Behavior of Rectangular Concrete-Filled Steel Tube Columns with Binding Bars. Journal of South China University of Technology (Natural Science Edition), 36(12), 21-27. (in Chinese)

Mangalathu, S., & Jeon, J. S. (2019). Machine learning–based failure mode recognition of circular reinforced concrete bridge columns: Comparative study. Journal of Structural Engineering, 145(10), 04019104.

Matsui, C. and Tsuda, K. (1996). Strength And Behavior of Slender Concrete Filled Steel Tubular Columns. Proceedings of The Second International Symposium on Civil Infrastructure Systems, Hong Kong, China.

Mirza, S. A., & Lacroix, E. A. (2004). Comparative strength analyses of concrete-encased steel composite columns. Journal of Structural Engineering, 130(12), 1941-1953.

Mursi, M., and Uy, B. (2004). Strength of slender concrete filled high strength steel box columns. Journal of Constructional Steel Research, 60(12), 1825–1848.

Naser, M. Z., Thai, S., & Thai, H. T. (2021). Evaluating structural response of concrete-filled steel tubular columns through machine learning. Journal of Building Engineering, 34, 101888.

Olalusi, O. B., & Awoyera, P. O. (2021). Shear capacity prediction of slender reinforced concrete structures with steel fibers using machine learning. Engineering Structures, 227, 111470.

Pedregosa, F., et al. (2011). Scikit-learn: Machine learning in Python. Journal of machine Learning research, 12, 2825-2830.

Platt, J. (1999). Probabilistic outputs for support vector machines and comparisons to regularized likelihood methods. Advances in large margin classifiers, 10(3), 61-74.

Prayogo, D., Cheng, M. Y., Wu, Y. W., & Tran, D. H. (2020). Combining machine learning models via adaptive ensemble weighting for prediction of shear capacity of reinforced-concrete deep beams. Engineering with Computers, 36(3), 1135-1153.

Qu, X., Chen, Z., and Sun, G. (2013). "Experimental study of rectangular CFST columns subjected to eccentric loading." Thin-Walled Structures, 64, 83–93.

Reineck, K. H., Kuchma, D. A., Kim, K. S., & Marx, S. (2003). Shear database for reinforced concrete members without shear reinforcement. Structural Journal, 100(2), 240-249.

Ren, Q., Li, M., Zhang, M., Shen, Y., & Si, W. (2019). Prediction of ultimate axial capacity of square concrete-filled steel tubular short columns using a hybrid intelligent algorithm. Applied Sciences, 9(14), 2802.

Sakino, K., Nakahara, H., Morino, S., & Nishiyama, I. (2004). Behavior of centrally loaded concrete-filled steel-tube short columns. Journal of structural engineering, 130(2), 180-188.

Shakir-Khalil, H. and Mouli, M. (1990). Further Tests on Concrete-Filled Rectangular Hollow-Section Columns. The Structural Engineer, 68(20), 405-413.

Shakir-Khalil, H. and Zeghiche, J. (1989). Experimental Behaviour of Concrete-Filled Rolled Rectangular Hollow-Section Columns. The Structural Engineer, 67, 346–353.

Tao, Z., Han, L.-H., and Wang, D.-Y. (2007). Experimental behaviour of concrete-filled stiffened thin-walled steel tubular columns. Thin-Walled Structures, 45(5), 517–527.

Tran, V. L., Thai, D. K., & Kim, S. E. (2019). Application of ANN in predicting ACC of SCFST column. Composite Structures, 228, 111332.

Uy, B. (2000). Strength of concrete filled steel box columns incorporating local buckling. Journal of structural engineering, 126(3), 341-352.

Uy, B. (2001). Strength of short concrete filled high strength steel box columns. Journal of Constructional Steel Research, 57(2), 113–134.

Wang, Y. C., and Moore, D. B. (1997). A design method for concrete-filled hollow section, composite columns. The Structural Engineer, 75(21), 368–373.

Wei Z, and Han L. (2000). Research on the bearing capacity of early-strength concrete filled square steel tube, Proceedings 6th ASCCS Conference: Composite and Hybrid Structures, Vol. 1, Los Angeles, pp. 395–402, 2000.

Xiong, M.-X., Xiong, D.-X., and Liew, J. Y. R. (2017). "Behaviour of steel tubular members infilled with ultra high strength concrete." Journal of Constructional Steel Research, 138, 168–183.

Yu, Q., Tao, Z., and Wu, Y.-X. (2008). "Experimental behavior of high-performance concrete-filled steel tubular columns." Thin-Walled Structures, 46(4), 362–370.

Zhang, J., Sun, Y., Li, G., Wang, Y., Sun, J., & Li, J. (2020). Machine-learning-assisted shear strength prediction of reinforced concrete beams with and without stirrups. Engineering with Computers, 1-15.

Zhang, S., and Guo, L. (2007). Behaviour of high strength concrete-filled slender RHS steel tubes. Advances in Structural Engineering, 10(4), 337–351.

Zhang, S., Guo, L., Wang, Y., and Tian, H. (2004). Experimental research and theoretical analysis of high strength concrete-filled square hollow section steel tubes subjected to eccentric loading. Journal of Building Structures, 25(1), 17-25. (in Chinese)

Zhang, Z. G.(1989). Research on basic behaviour of concrete filled square steel tubular stub under eccentric load. Journal of Building Structures, 10(6), 10-20. (in Chinese)

Zhong, Y., Sun, Y., Tan, K. H., & Zhao, O. (2021). Testing, modelling and design of high strength concrete-filled high strength steel tube (HCFHST) stub columns under combined compression and bending. Engineering Structures, 241, 112334.

Zhu, J. Y., & Chan, T. M. (2018). Experimental investigation on octagonal concrete filled steel stub columns under uniaxial compression. Journal of Constructional Steel Research, 147, 457-467.